HETE-2 Observations of the Extremely Soft X-Ray Flash XRF 020903

T.Sakamoto[1,2,3], D. Q. Lamb[4], C. Graziani[4], T. Q. Donaghy[4], M. Suzuki[1], G. Ricker[5], J-L. Atteia[6], N. Kawai[1,2], A. Yoshida[2,7], Y. Shirasaki[8], T. Tamagawa[2], K. Torii[2], M. Matsuoka[9], E. E. Fenimore[3], M. Galassi[3], T. Tavenner[10], J. Doty[5], R. Vanderspek[5], G. B. Crew[5], J. Villasenor[5], N. Butler[5], G. Prigozhin[5], J. G. Jernigan[11], C. Barraud[6], M. Boer[12], J-P. Dezalay[12], J-F. Olive[12], K. Hurley[11], A. Levine[5], G. Monnelly[5], F. Martel[5], E. Morgan[5], S. E. Woosley[13], T. Cline[14], J. Braga[15], R. Manchanda[16], G. Pizzichini[17], K. Takagishi[18], and M. Yamauchi[18]

ABSTRACT

We report HETE-2 WXM observations of the X-ray flash, XRF 020903. This event was extremely soft: the ratio $\log(S_X/S_\gamma) = 4.3$, where S_X and S_γ are the fluences in the 2-30 and 30-400 keV energy bands, is the most extreme value observed so far by HETE-2. In addition, the spectrum has an observed peak energy $E^{\rm obs}_{\rm peak} < 5.0$ keV (99.7% probability upper limit) and no photons were detected above ~ 10 keV. The burst is shorter at higher energies, which is similar

[1]Department of Physics, Tokyo Institute of Technology, 2-12-1 Ookayama, Meguro-ku, Tokyo 152-8551, Japan

[2]RIKEN (Institute of Physical and Chemical Research), 2-1 Hirosawa, Wako, Saitama 351-0198, Japan

[3]Los Alamos National Laboratory, P.O. Box 1663, Los Alamos, NM, 87545

[4]Department of Astronomy and Astrophysics, University of Chicago, IL, 60637

[5]Center for Space Research, Massachusetts Institute of Technology, 70 Vassar Street, Cambridge, MA, 02139

[6]Laboratoire d'Astrophysique, Observatoire Midi-Pyreńeés, 14 Ave. E. Belin, 31400 Toulouse, France

[7]Department of Physics, Aoyama Gakuin University, Chitosedai 6-16-1, Setagaya-ku, Tokyo 157-8572, Japan

[8]National Astronomical Observatory, Osawa 2-21-1, Mitaka, Tokyo 181-8588, Japan

[9]Tsukuba Space Center, National Space Development Agency of Japan, Tsukuba, Ibaraki, 305-8505, Japan

[10]Department of Astronomy, New Mexico State University, 1320 Frenger Mall, Las Cruces, NM, 88003-8001

[11]University of California at Berkeley, Space Sciences Laboratory, Berkeley, CA, 94720-7450

[12]Centre d'Etude Spatiale des Rayonnements, CNRS/UPS, B.P.4346, 31028 Toulouse Cedex 4, France

[13]Department of Astronomy and Astrophysics, University of California at Santa Cruz, 477 Clark Kerr Hall, Santa Curz, CA 95064

[14]NASA Goddard Space Flight Center, Greenbelt, MD, 20771

[15]Instituto Nacional de Pesquisas Espaciais, Avenida Dos Astronautas 1758, Saõ Josedos Campos 12227-010, Brazil

[16]Department of Astronomy and Astrophysics, Tata Institute of Fundamental Research, Homi Bhabha Road, Mumbai, 400 005, India

[17]Consiglio Nazionale delle Ricerche (IASF), via Piero Gobetti, 101-40129 Bologna, Italy

[18]Faculty of engineering, Miyazaki University, Gakuen Kibanadai Nishi, Miyazaki 889-2192, Japan

to the behavior of long GRBs. We consider the possibility that the burst lies at very high redshift and that the low value of $E_{\rm peak}^{\rm obs}$ is due to the cosmological redshift, and show that this is very unlikely. We find that the properties of XRF 020903 are consistent with the relation between the fluences $S(7-30\ {\rm keV})$ and $S(30-400\ {\rm keV})$ found by Barraud et al. for GRBs and X-ray-rich GRBs, and are consistent with the extension by a decade of the hardness-intensity correlation (Mallozzi et al. 1995) found by the same authors. Assuming that XRF 020903 lies at a redshift $z = 0.25$ as implied by the host galaxy of the candidate optical and radio afterglows of this burst, we find that the properties of XRF 020903 are consistent with an extension by a factor ~ 300 of the relation between the isotropic-equivalent energy $E_{\rm iso}$ and the peak $E_{\rm peak}$ of the νF_ν spectrum (in the source frame of the burst) found by Amati et al. for GRBs. The results presented in this paper therefore provide evidence that XRFs, X-ray-rich GRBs, and GRBs form a continuum and are a single phenomenon. The results also impose strong constraints on models of XRFs and X-ray-rich GRBs.

Subject headings: Gamma rays: bursts (GRB 020903)

1. Introduction

Gamma-ray bursts (GRBs) that have a large fluence in the X-ray energy band (2-30 keV) relative to the gamma-ray energy band (30-400 keV) are receiving increased attention. The Burst and Transient Source Experiment (BATSE) on board the *Compton Gamma Ray Observatory* detected 2704 GRBs (Paciesas et al. 1999). The spectra of 156 bright bursts exhibit a distribution of low-energy power-law indices α whose centroid is ~ -1, and a distribution of observed break energies $E_{\rm break}^{\rm obs}$ whose centroid is ≈ 230 keV (Preece et al. 2000), where $E_{\rm break}^{\rm obs} = (\alpha - \beta)(2+\alpha)^{-1} E_{\rm peak}^{\rm obs}$. Here α, β, and $E_{\rm peak}^{\rm obs}$ are the slope of the low-energy power-law index, the high-energy power-law index, and the energy of the peak of the νF_ν spectrum of the Band function (Band et al. 1993), an expression that satisfactorily represents the spectra of almost all GRBs. In contrast, 36% of the bright bursts observed by *GINGA* have peak energies $E_{\rm peak}^{\rm obs}$ in their photon number spectrum at a few keV and large X-ray to γ-ray fluence ratios (Strohmayer et al. 1998).

The *Beppo*SAX Wide Field Camera (WFC) detected events that are very similar to the soft *GINGA* GRBs; these events have been termed "X-ray Flashes" (XRFs) (Heise et al. 2000).[19] The energy flux of these XRFs lies in the range $10^{-8} - 10^{-7}$ erg cm^{-2} s^{-1} and the

[19]Throughout this paper, we define "X-ray-rich" GRBs and XRFs as those events for which $\log[S_X(2-$

low-energy photon index α of their spectra ranges from -3 to -1.2. The sky distribution of XRFs is consistent with isotropy, and there is no evidence that the sources are Galactic. The XRFs have t_{90} durations between 10 and 200 sec. The event rate of XRFs by the WFC is 3.4 events per year. Clarifying the connection between XRFs and GRBs could provide a breakthrough in our understanding of the prompt emission of GRBs.

Kippen et al. (2002) made a detailed spectral comparison of GRBs and XRFs, using a sample of eighteen GRBs that were observed by BATSE and a sample of nine XRFs that were observed by both the WFC and BATSE. According to their joint analysis of WFC/BATSE spectral data, the low-energy and high-energy photon indices of XRFs are -1 and ~ -2.5, respectively, which are no different from those of GRBs. On the other hand, XRFs have much lower values of $E^{\rm obs}_{\rm peak}$ than do GRBs. Thus the only temporal or spectral difference between GRBs and XRFs appears to be that XRFs have lower $E^{\rm obs}_{\rm peak}$ values. Kippen et al. therefore suggest that XRFs might represent an extension of the GRB population to events with low peak energies. Analyzing 35 HETE-2 GRBs seen by FREGATE, Barraud et al. (2003) demonstrate that the spectral properties of "X-ray rich" GRBs form a continuum with those of ordinary GRBs and suggest that XRFs may represent a further extension of this continuum.

BATSE's low-energy threshold of ~ 20 keV made it difficult for BATSE to detect XRFs. *Ginga* and *Beppo*SAX had the capability of detecting XRFs; however, *Ginga* could not determine the direction of the burst and the *Beppo*SAX GRBM had difficulty in triggering on XRFs. Consequently, these missions could not carry out in depth investigations of XRFs. In contrast, HETE-2 (Ricker et al. 2003) has the ability to trigger on and localize XRFs, and to study their spectral properties, using the Wide-Field X-Ray Monitor [WXM; 2-25 keV energy band; Kawai et al. (2003)] and the French Gamma Telescope [FREGATE; 6-400 keV energy band; Atteia et al. (2003)], which have energy thresholds of a few keV.

In this Letter, we report the detection and localization of XRF 020903 by HETE-2 (Ricker et al. 2002) and present the results of a detailed study of its properties. Since this event was extremely soft and there was very little signal (a $\sim 2\sigma$ excess in the best selected energy range) in FREGATE, we focus our analysis on the WXM temporal and spectral data for the event.

---

30 kev)/S_γ(30 − 400 kev)] > -0.5 and 0.0, respectively.

2. Observations

2.1. Localization

XRF 020903 was detected with the HETE-2 WXM and the Soft X-ray Camera [SXC; 0.5-10 keV energy band; Villasenor et al. (2003)] instruments at 10:05:37.96 UT on 2002 September 3 (Ricker et al. 2002). The WXM flight localization was correct, but was not sent out because HETE-2 was pointing at the Galactic Bulge region at the time and WXM triggers were therefore not being sent to the GCN in order not to overwhelm the astronomical community with X-ray burst localizations. A GCN Notice reporting the localization of the burst, based on ground analysis (Graziani et al. 2003; Shirasaki et al. 2003) of the WXM data, was sent out 231 minutes after the burst.

The WXM localization can be expressed as a 90% confidence circle that is 16.6′ in radius and is centered at R.A. = $22^{\rm h}49^{\rm m}25^{\rm s}$, Dec. = $-20°53'59''$ (J2000). A localization of the burst based on ground analysis (Monnelly et al. 2003) of the SXC data was distributed as a GCN Notice about 7 hours after the burst. Only a one-dimensional localization was possible using the SXC data, but this significantly reduced the area of the localization region for XRF 020903. The improved localization produced by combining the SXC and WXM localizations can be described as a 90% confidence quadrilateral that is 4′ in width and $\sim$31′ in length (see Figure 1). It is centered at R.A. = $22^{\rm h}49^{\rm m}01^{\rm s}$, Dec. = $-20°55'47''$ (J2000), and its four corners lie at (R.A., Dec.) = ($22^{\rm h}48^{\rm m}48.00^{\rm s}$, $-20°39'36.0''$), ($22^{\rm h}48^{\rm m}33.60^{\rm s}$, $-20°42'36.0''$), ($22^{\rm h}49^{\rm m}10.80^{\rm s}$, $-21°10'12.0''$), and ($22^{\rm h}49^{\rm m}30.00^{\rm s}$, $-21°10'48.0''$) (J2000).

Detection of candidate optical and radio afterglows of XRF 020903, and the host galaxy of the candidate optical and radio afterglows, have been reported. Soderberg et al. (2002) discovered an optical transient within the HETE-2 SXC + WXM localization region at R.A. = $22^{\rm h}48^{\rm m}42.34^{\rm s}$, Dec = $-20°46'09.3''$, using the Palomar 200-inch telescope. These authors mention that the optical transient brightened by $\sim 0.3-0.4$ magnitudes between about 7 and 24 days after the XRF, and suggest that the re-brightening might be due to an associated supernova. However, the optical transient apparently faded by over a magnitude only three days later (Covino et al. 2002). Spectroscopic observations of the optical transient, using the Magellan 6.5m Baade and Clay telescopes, detected narrow emission lines from an underlying galaxy at a redshift $z = 0.25 \pm 0.01$, suggesting that the host galaxy of the optical transient is a star-forming galaxy [Soderberg et al. (2002); see also Chornock & Filippenko (2002)]. A fading bright radio source at the position of optical transient was detected using the Very Large Array (Berger et al. 2002). Hubble Space telescope observations of the XRF 020903 field reveal the optical transient and show that its host galaxy is an irregular galaxy, possibly with four interacting components (Levan et al. 2002). These detections likely represent the first discoveries of the optical and radio afterglows, together with the host galaxy, of an XRF.

In our analysis of the prompt emission of XRF 020903, we apply a "cut" to the WXM photon time- and energy-tagged data (TAG data), using only the photons from the pixels on the three wires in the X-detectors (XA0, XA1, and XA2) and the four wires in the Y-detectors (YA1, YA2; YB0, YB1) that were illumnated by the burst *and* that maximize the S/N of the burst light curve, in the same manner as we did for GRB 020531 (Lamb et al. 2003). We use this optimized TAG data when performing our temporal and spectral analyses of this event.

2.2. Temporal Properties

Figure 2 shows the light curve of XRF 020903 in four WXM energy bands. The time history of the burst in the 2-5 and 5-10 keV energy bands has two peaks. Clearly, there is no significant flux above 10 keV. Table 1 gives the t_{50} and t_{90} durations of the burst in the 2-5 keV, 5-10 keV, and 2-10 keV energy bands. The duration of the burst is longer in the lower energy band; this trend is similar to that seen in long bright GRBs (Fenimore et al. 1995).

2.3. Spectrum

As we have seen, the light curve of XRF 020903 shows two peaks: the first occurring in the time interval 0-8 s, and the second occurring in the time interval 8-13 s. The S/N of the first peak is much higher than that of the second. In addition, inspection of the burst light curve in the 2-5 and 5-10 keV energy bands suggests that the second peak is much softer than the first. For these reasons, we analyze the spectrum of the burst in three time intervals: 0-8 s, 8-13 s, and the total duration of the burst, 0-13 s. The background region we use is 40 seconds in duration and starts 45 seconds before the burst.

The WXM detector response matrix has been well-calibrated using observations of the Crab nebula (Shirasaki et al. 2002). In the spectral fits, we include only the photons that registered on the three wires in the X-detectors and the four wires in the Y-detectors that were illuminated by the burst, as mentioned above. Since the variation in the gain is not uniform at the ends of the wires in the WXM detectors (Shirasaki et al. 2000), we use only the photon counts that registered in the central ± 50 mm region of the wires to construct the spectra of the burst. We include all of the photons that register in the central regions of these wires (i.e, we use the full 2-25 keV energy range of the WXM). The relation between pulse height and energy in the WXM is non-linear and is different for each wire. In order to extract the strongest possible constraints on the parameters of the spectral models we consider, we treat each individual WXM wire separately but take the normalizations on all wires to be the same. For the same reason, we do not re-bin any of the pulse height channels in the WXM and in the FREGATE, and we carry out a set of fits for the total duration of the burst (0-13 s) that include the spectral data from both the WXM and the FREGATE. We use the XSPEC v11.2.0 software package to do the spectral fits.

Table 2 presents the results of our time-resolved and time-integrated spectral analysis of the burst. In this analysis, we consider the following models: (1) blackbody, (2) power-law model with a photo-electric absorption, (3) power-law times exponential (PLE) [the COMP model in Preece et al. (2000)], and (4) Band function (Band et al. 1993) with photo-electric absorption. In some models, we fix the value of N_H to the Galactic value, 2.3×10^{20} cm^{-2} (Dickey & Lockman 1990); in the Band model fits, we have fixed $\alpha = -1$, which is a typical value for GRBs, in order to better constrain the remaining parameters. All of the models provide acceptable fits to the data; i.e., the data do not request models more complicated than a blackbody or a power-law.

However, essentially all GRB spectra are well-described by the Band function (Band et al. 1993; Preece et al. 2000), and the analysis of Kippen et al. (2002) shows that at least some XRF spectra are also well-described by the Band function. Fits to the WXM data for all three time intervals using the power-law model give spectral slopes $\alpha < -2$ with high significance. For example, comparing the minimum value $\chi^2_{\rm min} = 53.4$ corresponding to the best-fit value of the spectral slope $\alpha = -2.8$ and the value $\chi^2 = 60.6$ at $\alpha = -2$ for the power-law fit to the average spectrum of the burst (i.e., the time interval 0-13 s), we find that $\Delta\chi^2 = 7.2$ for one additional parameter. Thus, using the Maximum Likelihood Ratio Test, $\alpha < -2$ at the 99.3% confidence level. From this evidence, we conclude that the peak $E_{\rm peak}$ in νF_ν lies near or below 2 keV, the lower limit of the energy range of the WXM detectors.

There is evidence of spectral softening between the first and second time intervals. In particular, a power-law fit to the first time interval gives $\alpha_1 = -2.4^{+0.5}_{-0.6}$ and $\chi^2_{\rm min,1} = 75.1$, while a power-law fit to the second time interval gives $\alpha_2 = -4.2^{+1.1}_{-3.7}$ and $\chi^2_{\rm min,2} = 71.1$. In contrast, a power-law fit to the first and second time intervals, but with $\alpha = \alpha_1 = \alpha_2$ gives $\alpha = -2.86^{+0.44}_{-0.82}$ and $\chi^2_{\rm min} = 152.2$. The first (more complicated) model includes the second model as a special case (i.e., the models are nested). Comparing $\chi^2_{\rm min}$ for the two models, we find that $\Delta\chi^2 = 6.0$ for one additional parameter. Thus, using the Maximum Likelihood Ratio Test , there is evidence of spectral softening at the 98.6% confidence level.

Figure 3 shows a comparison of the observed count spectrum and the count spectrum predicted by the best-fit power-law model, for the time intervals 0-8 s and 8-13s. Figure 4 shows the same comparison, except for the total duration of the burst (0-13 s). Table 3 gives the peak photon number and energy fluxes (in 1 s) and the fluence of XRF 020903, assuming the power-law model.[20]

Using the best-fit power-law model for the average spectrum of the burst, we find fluences $S_X(2-30 \text{ keV}) = 7.2 \times 10^{-8}$ erg cm^{-2} and $S_\gamma(30-400 \text{ keV}) = 3.4 \times 10^{-12}$ erg cm^{-2}. Thus the ratio of fluences $\log[S_X(7-30 \text{ keV})/S_\gamma(30-400 \text{ keV})] = 4.3$, making this burst not only an XRF but the most extreme example of an XRF observed so far by HETE-2.

A comparison of the power-law and Band function fits to the first peak, which has a much higher S/N than the second peak, provides modest evidence for an $E^{\rm obs}_{\rm peak}$ near 2 keV, the lower limit of the energy range of the WXM detectors. Specifically, we find that$\Delta\chi^2 = 4.34$ for one additional parameter, which means that the data requests the (more complicated) Band function model at the 89% confidence level. However, the evidence is clearly not of high statistical significance, and in this fit we fixed α at -1, its typical value for GRBs.

We therefore choose to place an upper limit on $E^{\rm obs}_{\rm peak}$. The appropriate model to use is the Band function, since (as we have already mentioned) the spectra of almost all GRBs and at least some XRFs are well-described by this function. However, this presents a problem: the Band function has two distinct ways of representing a power-law spectrum in the detector energy range. First, it can do so by having $E_{\rm break} \to 0$, so that only the high-energy, pure power-law part of the Band function is visible in the energy range of the detector. Second, it can do so by having $E_{\rm break} \to \infty$ and $E_0 \to \infty$, where E_0 is the "cutoff energy" of the cutoff power-law that constitutes the low-energy part of the Band function. In this limit, the limiting power-law is actually the cutoff power-law, but the cutoff energy is so large that the curvature of the model is imperceptible in the detector energy range.

We solve this problem by developing a new statistical method. This method uses a *constrained* Band function which is parameterized by two quantities, $E^{\rm obs}_{\rm peak}$ and β. The *constrained* Band function is perfectly able to make both pure power-law spectra and power-law times exponential spectra of the required curvature in the detector energy range, but only the high-energy part of the Band function is allowed to produce a pure power-law spectrum.

---

[20]We compute the peak photon number flux in the WXM 2-5, 5-10, and 2-10 keV energy bands, using the best-fit power-law model parameters for the average photon energy spectrum of the burst, and the ratio 2.731 of the photon flux in the 1 s time interval containing the largest number of photons and the average photon flux in the 0 - 13 s time interval. We compute the peak photon energy flux in the WXM 2-5, 5-10, and 2-10 keV energy bands in exactly the same way, except that we use the ratio 3.247 of the total photon energy flux (found by weighting each photon with its energy and summing the energies) found in the 1 s time interval containing the largest total photon energy and the average photon energy flux in the 0 - 13 s time interval.

We describe this new method in detail in Appendix A. This method has general applicability to all instruments when the spectra of the bursts considered have $E^{\rm obs}_{\rm peak}$ near or below the low-energy threshold of the detector.

Figure 5 shows the posterior probability density distribution for $E^{\rm obs}_{\rm peak}$ we find using this approach. From this posterior probability density distribution, we find a best-fit value $E^{\rm obs}_{\rm peak} = 2.7$ keV, that 1.1 keV $< E^{\rm obs}_{\rm peak} <$ 3.6 keV with 68% probabilty, and that $E^{\rm obs}_{\rm peak} < 4.1$ and 5.0 keV with 95% and 99.7% probabilities.

We conclude that the properties of XRF 020903 are very similar to those of long GRBs, with the exception that the observed peak energy $E^{\rm obs}_{\rm peak} \sim 3$ keV is $\sim$ 100 times smaller. The extremely low value of $E^{\rm obs}_{\rm peak}$ seen in XRF 020903 is similar to the smallest value found among the 9 XRFs whose spectra were determined by jointly fitting *Beppo*SAX WFC and BATSE data (Kippen et al. 2002).

3. Discussion

3.1. Source Properties

We exclude the possibility that XRF 020903 is a Type I X-ray burst (XRB) on the following grounds. First, its galactic latitude is $b = -61.5^\circ$ (using the center of the combined WXM plus SXC error box), and there is no known persistent X-ray source or globular cluster in this error box. Since Type I X-ray burst sources lie in the Galactic plane or in globular clusters, and have persistent X-ray emission, XRF 020903 is unlikely to be an X-ray burst on locational grounds alone. Second, the time history of XRF 020903 is not FRED-like (i.e., it does not exhibit a fast rise and an exponential decay), while those of XRBs typically are. Third, although the blackbody model gives an acceptable fit to the spectra of the first and second peaks in the time history of XRF 020903, the derived blackbody temperatures are $\sim$ 1.0 keV. These temperatures are lower than those of almost all Type I X-ray bursts [which typically have temperatures $T \approx 2$ keV; see, e.g. Lewin, van Paradijs & Taam (1993)]. For these reasons, we conclude that XRF 020903 is an XRF and not an XRB.

The extremely low value of $E^{\rm obs}_{\rm peak}$ observed for XRF 020903 is remarkable. If the observed spectrum of XRF 020903 were the redshifted spectrum of a typical GRB, the implied redshift would be $z \sim 100$, using the best-fit value of $E^{\rm obs}_{\rm peak} = 2.7$ keV observed for XRF 020903 and the mean value of $E^{\rm obs}_{\rm break}$ for the sample of 5500 spectra formed from the brightest 156 BATSE GRBs (Preece et al. 2000). A redshift of this magnitude would be hard to understand, and is certainly not expected if long GRBs are associated with the collapse of massive stars (Lamb & Reichart 2000). It is also wildly inconsistent with the measured redshift $z = 0.25$ of the host galaxy (Soderberg et al. 2002) of the candidate optical (Soderberg et al. 2002) and radio (Berger et al. 2002) afterglows of XRF 020903. It is therefore difficult to attribute the low observed value of $E^{\rm obs}_{\rm peak}$ for XRF 020903 to cosmological redshift.

3.2. Fluence and Peak Energy Correlations

In Figure 6, we plot XRF 020903 in the (S_{30-400},S_{7-30})-plane, where S_{7-30} and S_{30-400} are the energy fluences of the bursts in the 7-30 and 30-400 keV energy bands. For the value of S_{7-30}, we use the best-fit power-law model for the average spectrum of the burst, extrapolated through the 7-30 keV energy range. For S_{30-400}, we use the 3σ upper limit from the FREGATE data, which we estimate to be $\approx 2.1 \times 10^{-8}$ erg cm^{-2}. Also plotted in this figure are the 35 GRBs whose spectra have been determined using HETE-2 FREGATE data (Barraud et al. 2003). Figure 6 shows that the properties of XRF 020903 are consistent with the relation between S_{7-30} and S_{30-400} found by Barraud et al. (2003).

In Figure 7, we plot XRF 020903 in the (S_{2-400},$E^{\rm obs}_{\rm peak}$)-plane, where $E^{\rm obs}_{\rm peak}$ is the peak of the observed νF_ν spectrum. For $E^{\rm obs}_{\rm peak}$, we plot the 99.7% upper limit (5.0 keV). The properties of XRF 020903 are consistent with an extension by two decades of the hardness-intensity correlation (Mallozzi et al. 1995; Lloyd-Ronning, Petrosian & Mallozzi 2000) between S_{30-400} and $E^{\rm obs}_{\rm peak}$ found by Barraud et al. (2003).

Assuming that the candidate optical and radio afterglows of XRF 020903 are indeed the afterglows of XRF 020903, and therefore that the redshift of the underlying host galaxy is the redshift of the XRF, we can calculate the isotropic-equivalent radiated energy $E_{\rm iso}$ and the upper limit on the peak energy $E_{\rm peak}$ of the νF_ν spectrum in the source frame in the same way as Amati et al. (2002). Figure 8 shows that the properties of XRF 020903 are consistent with an extension by a factor of ~ 300 in $E_{\rm iso}$ of the relation found by Amati et al. (2002).

Figures 6 - 8 provide evidence that XRFs, "X-ray-rich GRBs," and GRBs form a continuum, and are therefore the same phenomenon.

3.3. Constraints on Theoretical Models of XRFs

A variety of theoretical models have been proposed to explain XRFs [see, e.g., Zhang & Mészáros (2003) for a comparative discussion of several of these models]. In the off-axis GRB jet model (Yamazaki, Ioka, & Nakamura 2002, 2003), XRFs are the result of viewing the jet of an ordinary GRB off-axis, so that relativistic beaming shifts the γ-rays into the

X-ray range. In the clean fireball model, XRFs are due to the relativistic pair plasma in the GRB jet becoming optically thin much later than usual, at which time the relativistic bulk Lorentz factor Γ has already decreased to a relatively low value (Mochkovitch et al. 2003). In the dirty fireball model, XRFs occur when there is significant baryon loading of the GRB jet, so that Γ never reaches large values (Dermer, Chiang, & Böttcher 1999; Huang, Dai, & Lu 2002). In the universal jet model, XRFs are the result of viewing the GRB jet off-axis, where Γ is lower because of the structure of the jet (Rossi, Lazzati, & Rees 2002; Woosley, Zhang, & Heger 2003; Zhang & Mészáros 2002; Mészáros, Ramirez-Ruiz, Rees, & Zhang 2002). In the uniform jet model, the different properties of XRFs, "X-ray-rich" GRBs, and GRBs are due primarily to different jet opening angles, with larger jet opening angles associated with lower values of Γ (Lamb, Donaghy & Graziani 2003).

Any such model of XRFs must reproduce the correlation found by Barraud et al. (2003) between S_{7-30} and S_{30-400}, and the evidence we report in this paper for correlations between S_{2-400} and $E_{\rm peak}^{\rm obs}$, and especially, $E_{\rm iso}$ and $E_{\rm peak}$ – the latter spanning nearly five decades in $E_{\rm iso}$.

4. Conclusions

In this paper, we have reported HETE-2 WXM observations of the X-ray flash, XRF 020903. This event was extremely soft: the spectrum had a best-fit peak energy $E_{\rm peak}^{\rm obs} = 2.7$ keV and $E_{\rm peak}^{\rm obs} < 5.0$ keV (99.7% probability upper limit) and no photons were detected above ~ 10 keV. The burst is shorter at higher energies, which is typical of long GRBs. We considered the possibility that the burst lies at very high redshift and that the low value of $E_{\rm peak}^{\rm obs}$ is therefore due to the cosmological redshift, and showed that this is very unlikely. We find that the properties of XRF 020903 are consistent with the relation between S_{7-30} and S_{30-400} found by Barraud et al. (2003) for GRBs and X-ray-rich GRBs, and are consistent with an extension by two decades of the hardness-intensity correlation (Mallozzi et al. 1995; Lloyd-Ronning, Petrosian & Mallozzi 2000) between S_{30-400} and $E_{\rm peak}^{\rm obs}$ demonstrated by the same authors. Assuming that XRF 020903 lies at a redshift $z = 0.25$ as implied by the host galaxy of the candidate optical afterglow of this burst, we find that the the properties of XRF 020903 are consistent with an extension by a factor ~ 300 of the relation between $E_{\rm iso}$ and $E_{\rm peak}$ in the source frame of the burst found by Amati et al. (2002) for GRBs. When combined with earlier results, the results reported in this paper provide strong evidence that XRFs, X-ray-rich GRBs, and GRBs form a continuum and are a single phenomenon. The correlation found by Barraud et al. (2003) between S_{7-30} and S_{30-400}, and the evidence we find in this paper for correlations between S_{30-400} and $E_{\rm peak}^{\rm obs}$, and especially, $E_{\rm iso}$ and $E_{\rm peak}$, provide strong constraints on any model of XRFs and X-ray-rich GRBs.

We would like to thank the anonymous referee for comments and suggestions that materially improved the paper. The HETE-2 mission is supported in the U.S. by NASA contract NASW-4690; in Japan, in part by the Ministry of Education, Culture, Sports, Science, and Technology Grant-in-Aid 12440063; and in France, by CNES contract 793-01-8479. K. Hurley is grateful for *Ulysses* support under contract JPL 958059 and for HETE-2 support under contract MIT-SC-R-293291. G. Pizzihini acknowledges support by the Italian Space Agency. One of the authors (TS) is partially supported by the Junior Research Associate (JRA) program at RIKEN.

A. The "Constrained" Band Function For Soft GRBs

In the spectral analysis of GRBs, one occasionally encounters events (such as XRF 020903) that are so soft that they present themselves as pure power-laws with power-law index $\beta < -2$ in the energy range of the detector. The natural interpretation of such spectra is that the break energy $E_{\rm break}$ separating the two functional parts of the Band function is near or below the lower boundary of the detector energy range.

This situation creates a problem for fits of the Band function, in that the Band function has two distinct ways of conforming to a power-law in the detector energy range:

1. $E_{\rm break} \rightarrow 0$, so that only the high-energy, pure power-law part of the Band function is visible in the energy range of the detector.
2. $E_{\rm break} \rightarrow \infty$, $E_0 \rightarrow \infty$, where E_0 is the "cutoff energy" of the cutoff power-law that constitutes the low-energy part of the Band function. In this limit, the limiting power-law is actually the cutoff power-law, but the cutoff energy is so large that the curvature of the model is imperceptible in the detector energy range.

Therefore, despite the fact that the numerical value of the power-law index is such that we are certain that we should be dealing with the high-energy part of the Band function (i.e., the index is < -2, the low-energy part of the function can "horn in" on the fit, altering the physical inferences drawn from the spectrum.

This situation is particularly a problem for the estimation of $E_{\rm peak}$. Since we know that we are in case 1, we also know that we ought to have at least a firm upper limit on $E_{\rm peak}$, since $E_{\rm peak}$ is always necessarily less than $E_{\rm break}$, which is at the low end of the detector energy range. On the other hand, the case 2 limit implies $E_{\rm peak} \rightarrow \infty$. Unfortunately, the data doesn't care which side of the Band function makes the power-law, so no discrimination is possible between the two cases. Consequently, we can't constrain $E_{\rm peak}$ at all using a normal Band function fit.

The approach we have chosen to deal with this situation in the case of XRF 020903 is to fit a *constrained* Band function to the data. That is, we consider a three-dimensional subspace of the full four-dimensional Band function parameter space, choosing the subspace with a view to satisfying the following criteria:

1. It is perfectly possible to make both pure power-laws and cutoff power-laws of the any desired curvature in the detector energy range.
2. Only the high-energy part of the Band function is allowed to produce a pure power-law.

We define the three-dimensional subspace in the following way: consider a Band function parametrized by low- and high-energy indices α and β, and by a cutoff energy E_0. The well-known relation between E_0 and $E_{\rm break}$ is $E_{\rm break} = (\alpha - \beta)E_0$. We impose the constraint condition on our family of fitting functions

$$E_{\rm break} = E_{\rm pivot} \times (E_0/E_{\rm pivot})^{-1}, \tag{A1}$$

where $E_{\rm pivot}$ is some suitably chosen energy, in the general neighborhood where the GRB has appreciable emission. $E_{\rm break}$ and E_0 are then inversely related, and are equal to each other when both are equal to $E_{\rm pivot}$.

When $E_0 < E_{\rm pivot}$, then $E_{\rm break} > E_{\rm pivot}$, and the function is essentially a cutoff power-law in the energy range of interest.

On the other hand, when $E_0 > E_{\rm pivot}$, then $E_{\rm break} < E_{\rm pivot}$, and as $E_0 \rightarrow \infty$, $E_{\rm break} \rightarrow 0$. In other words, when the low-energy part of the Band function is trying to imitate a power law, the break energy becomes small enough to force the low-energy part of the function below the energy range of interest, where it cannot be seen and therefore can do no harm. Any pure power-law work must thus be done by the high-energy part of the Band function.

The resulting spectral function has three parameters (including the scale), rather than four. The two input shape parameters can be chosen arbitrarily from the set $\{\alpha, \beta, E_0, E_{\rm break}, E_{\rm peak}\}$. The remaining parameters may then be determined by algebraic relationships.

We have found it most convenient to adopt $E_{\rm peak}$ and β as our parameters. The choice of $E_{\rm peak}$ is dictated by the necessity of estimating its value, or at least an upper bound on its value. The choice of β is convenient because one may then impose the parameter bound $\beta < -2$, which guarantees that the formal expression for $E_{\rm peak}$ may be meaningfully interpreted as the energy of the peak of the νF_ν distribution. This bound on β is an important part of the specification of the fitting family of models. Were it not imposed, it would be possible for the formal expression for $E_{\rm peak}$ to exceed $E_{\rm break}$, so that at large values of $E_{\rm peak}$ the fit could always produce a $\beta \gtrsim -2$ power-law in the detector energy range. The result would be an extended tail of constant χ^2 for arbitrarily large values of $E_{\rm peak}$.

Figure 9 shows the constrained Band function, with $\beta = -2.5$ and $E_{\rm pivot} = 4$ keV, for different values of $E_{\rm peak}$. This figure shows that $E_{\rm peak}$ increases, $E_{\rm break}$ also necessarily increases, so that E_0 is forced to smaller and smaller values by the constraint, which increases the curvature (and the value of α).

Figure 10 shows the constrained Band function, with $E_{\rm peak} = 4$ keV and $E_{\rm pivot} = 4$ keV, for different values of β. The progression from some curvature at low energy ($\beta = -2.0$) to almost none ($\beta = -4.0$) is evident, as is the fact that as the curvature disappears, the resulting power-law is produced by the high-energy part of the Band function.

Figures 9 and 10 show that the constrained Band function is perfectly able to make both pure power-laws, and cutoff power-laws with any desired curvature in the detector energy range. Figure 10 demonstrates that, in the constrained Band function, a power-law spectrum is always produced by the high-energy part of the Band function.

The choice of $E_{\rm pivot}$ is dictated by the following considerations:

1. $E_{\rm pivot}$ must be low enough to prevent the low-energy part of the Band function from making a power-law in the energy range of interest. If $E_{\rm pivot}$ were 1 GeV (say), then the Band function would have no difficulty making E_0 large and $\alpha \lesssim -2$, which is what we are trying to prevent by introducing the constraint. So $E_{\rm pivot}$ should be "as low as possible."

2. $E_{\rm pivot}$ must not be so low that we cannot adequately fit any curvature that may exist in the spectrum. If $E_{\rm pivot}$ were 1 eV (say), then whenever $E_{\rm break}$ was in or above the energy range where the spectrum is appreciable, E_0 would be so tiny that the curvature of the model would be huge, much too large to fit the data well.

One way of choosing $E_{\rm pivot}$ is to calculate it's value using the best-fit parameters from a fit of a *free* Band function, using $E_{\rm pivot} = (E_0 E_{\rm break})^{1/2}$. This choice, which effectively chooses the unique constrained subspace of the full parameter space that contains the best-fit free Band function, allows the constrained family of functions to optimally fit whatever curvature the data may seem to hint is required.

We must require that the inferences that we draw from the spectral fit should be robust, in the sense that they should not depend strongly on the specific choice of $E_{\rm pivot}$. So the proper use of this constrained Band model involves not only choosing a representative value of $E_{\rm pivot}$, but also varying $E_{\rm pivot}$ in some reasonable range, to make sure that the conclusions about parameter estimates and bounds are unaffected by the choice of $E_{\rm pivot}$.

Figure 11 shows the constrained Band function, with $E_{\rm peak} = 4$ keV and $\beta = 2.0$, for different values of $E_{\rm pivot}$. Once again, as the low-energy curvature disappears, the resulting power-law is produced by the high-energy part of the Band function. Figure 11 also shows that the shape of the spectrum in the detector energy range is insensitive to the specific choice of $E_{\rm pivot}$, within a reasonable range. Thus the conclusions about parameter estimates and bounds are unaffected by the choice of $E_{\rm pivot}$.

Figure 12 shows the constrained Band functions with parameters that best fit the 13 s spectrum of XRF 020903, for different fixed values of $E_{\rm pivot}$. This figure illustrates the fact that the shape of the best-fit model is essentially unchanged in the energy range of the WXM for choices of $E_{\rm pivot}$ within a reasonable range.‘

Finally, we give the algebraic relationships necessary to recover the remaining Band function parameters assuming that $E_{\rm peak}$ and β are given. Let $x \equiv E_{\rm peak}/E_{\rm pivot}$. Then,

$$\alpha = -2 + \frac{1}{2}x^2 + \sqrt{\frac{1}{4}x^4 - x^2(\beta + 2)}, \tag{A2}$$

$$E_0 = (2 + \alpha)E_{\rm peak}. \tag{A3}$$

In Equation (A2), we have resolved the ambiguity in the choice of root of a quadratic equation by requiring that when $\beta + 2 < 0$, then $\alpha + 2 > 0$, so that $E_{\rm peak}$ is in fact the peak energy of the νF_ν distribution.

REFERENCES

Amati, L., et al. 2002, A&A, 390, 81

Atteia, J-L, et al. 2003, in Gamma-Ray Bursts and Afterglow Astronomy, eds. G. R. Ricker and R. Vanderspek (New York: AIP), 17

Band, D. L., et al. 1993, ApJ, 413, 281

Barraud, C., et al. 2003, A&A, 400, 1021

Berger, E., Kulkarni, S. R., Frail, D. A., Soderberg, Price, P. A., Fox, D. W., Harrison, F. A., & Yost, S. 2002, GCN Circ. 1555

Chornock, R., and Filippenko, A. V. 2002, GCN Circular 1609

Covino, S., et al, 2002, GCN Circ. 1563

Dermer, C. D., Chiang, J., & Böttcher, M. 1999, ApJ, 513, 656

Dickey & Lockman 1990 ARAA, 28, 215

Fenimore, E. E., in't Zand, J. J. M., Norris, J. P., Bonnell, J. T., & Nemiroff, R. J. 1995, ApJ, 448, L101

Graziani, C., et al. 2003, in Gamma-Ray Bursts and Astronomy, eds. G. R. Ricker and R. Vanderspek (New York: AIP), 114

Heise, J., in't Zand, J., Kippen, R. M., & Woods, P. M., in Proc. 2nd Rome Workshop: Gamma-Ray Bursts in the Afterglow Era, eds. E. Costa, F. Frontera, J. Hjorth (Berlin: Springer-Verlag), 16

Huang, Y. F., Dai, Z. G. & Lu, T. 2002, MNRAS, 332, 735

Kawai, N., et al. 2003, in Gamma-Ray Bursts and Afterglow Astronomy, eds. G. R. Ricker and R. Vanderspek (New York: AIP), 25

Kippen, R. M., Woods, P. M., Heise, J., in't Zand, J., Briggs, M. S., & Preece, R. D. 2002, in Gamma-Ray Bursts and Afterglow Astronomy, eds. G. R. Ricker and R. Vanderspek (New York: AIP), 244

Lamb, D. Q. et al. 2003, submitted to ApJ(astro-ph/0206151)

Lamb, D. Q. & Reichart, D. E. 2000, ApJ, 536, 1

Lamb, D. Q., Donaghy, T. Q., and Graziani, C. 2003, to be submitted to ApJ

Levan, A., Fruchter, A., Strolger, L., Burud, I., & Rhoads, J. 2002, GCN Circ. 1761

Lewin, W. H. G., van Paradijs, J.& Taam, R. E. 1993, Space Sci. Rev., 62, 223

Lloyd-Ronning, N., Petrosian, V., & Mallozzi, R. S. 2000, ApJ, 534, 227

Mallozzi, R. S., Paciesas, W. S., Pendleton, G. N., Briggs, M. S., Preece, R. D., Meegan, C. A. & Fishman, G. J. 1995, ApJ, 454, 597

Mészáros, P., Ramirez-Ruiz, E., Rees, M. J., & Zhang, B. 2002, ApJ, 578, 812

Monnelly, G., et al. 2003, in Gamma-Ray Bursts and Afterglow Astronomy, eds. G. R. Ricker and R. Vanderspek (New York: AIP), 25

Mochkovitch, R., Daigne, F., Barraud, C., & Atteia, J. L. 2003, ASP Conference Series (San Francisco: ASP), in press (astro-ph/0303289)

Paciesas, W. S., et al. 1999, ApJS, 122, 465

Preece, R. D., Briggs, M. S., Mallozzi, R. S., Pendleton, G. N., & Paciesas, W. S. 2000, ApJS, 126, 19

Ricker, G. R., et al. 2002, GCN Circ. 1530

Ricker, G. R., et al. 2003, in Gamma-Ray Bursts and Astronomy, eds. G. R. Ricker and R. Vanderspek (New York: AIP), 3

Rossi, E., Lazzati, D., & Rees, M. J. 2002, MNRAS, 332, 945

Shirasaki, Y., et al. 2000, SPIE, 4012, 166

Shirasaki, Y., et al. 2002, SPIE in press.

Shirasaki, Y., et al. 2003, in Gamma-Ray Bursts and Astronomy, eds. G. R. Ricker and R. Vanderspek (New York: AIP), 117

Soderberg, A. M., et al. 2002, GCN Circ. 1554

Strohmayer, T. E., Fenimore, E. E., Murakami, T., & Yoshida, A. 1998, ApJ, 500, 873

Villasenor, J. N., et al. 2003, in Gamma-Ray Bursts and Astronomy, eds. G. R. Ricker and R. Vanderspek (New York: AIP), 33

Woosley, S. E., Zhang, W. & Heger, A. 2003, ApJ, submitted (astro-ph/0206004)

Yamazaki, R., Ioka K. & Nakamura T. 2002, ApJ, 571, L31

Yamazaki, R., Ioka K. & Nakamura T. 2003, ApJ, submitted (astro-ph/0212557)

Zhang, B. & Mészáros, P. 2002, ApJ, 571, 876

Zhang & Mészáros, P. 2003, ApJ, in press (astro-ph/0206158)

This preprint was prepared with the AAS LaTeX macros v5.0.

Table 1: Temporal properties of XRF 020903.

Energy Band (keV)	t_{50} (s)	t_{90} (s)
2 - 5	5.8±0.9	10.6±0.2
5 - 10	2.4±0.2	4.3±2.2
2 - 10	4.9±0.6	9.8±0.6

Note.—The quoted errors correspond to $\pm 1\sigma$.

Table 2. Results of fits to the spectrum of XRF 020903.

Time region (s)	Model	N_H (10^{22} cm^{-2})	kT (keV)	α	β	$E_{\rm peak}^{\rm obs}$ (keV)	χ^2_ν (DOF)
0.0-8.0	blackbody		$1.04^{+0.24}_{-0.20}$				1.08 (62)
	power-law			$-2.4^{+0.5}_{-0.6}$			1.21 (62)
	cutoff power-law	0.023 (fixed)		-1.0 (fixed)		$3.1^{+1.9}_{-1.1}$	1.14 (62)
	Band	0.023 (fixed)		-1.0 (fixed)	< -2.4	$3.3^{+1.7}_{-1.3}$	1.16 (61)
8.0-13.0	blackbody		$0.54^{+0.23}_{-0.23}$				1.13 (62)
	power-law			$-4.2^{+1.1}_{-3.7}$			1.15 (62)
	cutoff power-law	0.023 (fixed)		-1.0 (fixed)		< 2.0	1.14 (62)
	Band	0.023 (fixed)		-1.0 (fixed)	< -3.3	< 2.0	1.16 (61)
0.0-13.0	blackbody		$0.87^{+0.20}_{-0.16}$				0.79 (62)
	power-law			$-2.8^{+0.5}_{-0.6}$			0.86 (62)
	cutoff power-law	0.023 (fixed)		-1.0 (fixed)		$2.4^{+1.2}_{-0.8}$	0.81 (62)
	Band	0.023 (fixed)		-1.0 (fixed)	< -2.5	$2.5^{+1.1}_{-0.9}$	0.82 (61)
0.0-13.0	blackbody		$0.90^{+0.21}_{-0.17}$				0.85 (177)
(with FREGATE)	power-law			$-2.6^{+0.4}_{-0.5}$			0.86 (177)
	cutoff power-law	0.023 (fixed)		-1.0 (fixed)		$2.6^{+1.4}_{-0.8}$	0.85 (177)
	Band	0.023 (fixed)		-1.0 (fixed)	< -2.3	< 4.1	0.86 (176)

Note.—The quoted errors correspond to the 90% confidence region

Table 3: Peak photon number and energy fluxes (in 1 s) and fluences in various energy bands for XRF 020903.

	2-5 keV	5-10 keV	2-10 keV
Peak flux (ph cm^{-2} s^{-1})	1.9 ± 0.7	$0.33^{+0.19}_{-0.16}$	2.2 ± 0.8
Peak flux (10^{-9} ergs cm^{-2} s^{-1})	$10.4^{+3.6}_{-3.7}$	$4.3^{+2.3}_{-2.2}$	14.7 ± 5.3
Total fluence (10^{-8} ergs cm^{-2})	4.2 ± 0.9	$1.7^{+0.8}_{-0.7}$	5.9 ± 1.4

Note.—All of the quantities in this table are derived assuming a power-law model for the spectrum. The quoted errors correspond to the 90% confidence region.

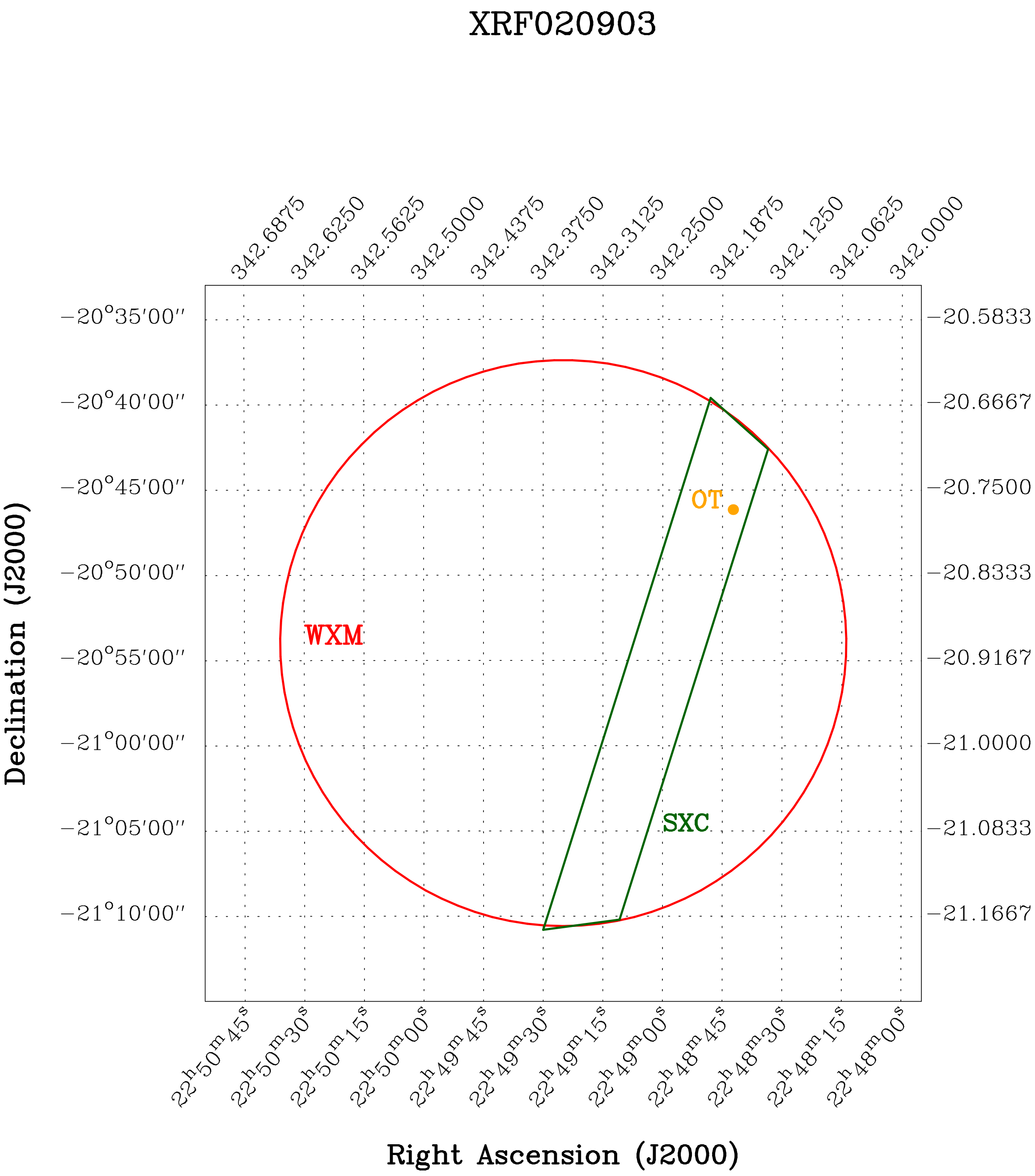

Fig. 1.— The HETE-2 WXM/SXC localization for XRF 020903. The circle is the 90% confidence region for the WXM localization and the belt-like region is the portion of the 90% confidence region for the one-dimensional SXC localization that lies within the WXM 90% confidence circle. The final localization is the intersection of the WXM and SXC localizations (Ricker et al. 2002a). The point labeled "OT" is the location of the candidate optical (Soderberg et al. 2002) and radio (Berger et al. 2002) afterglows of XRF 020903.

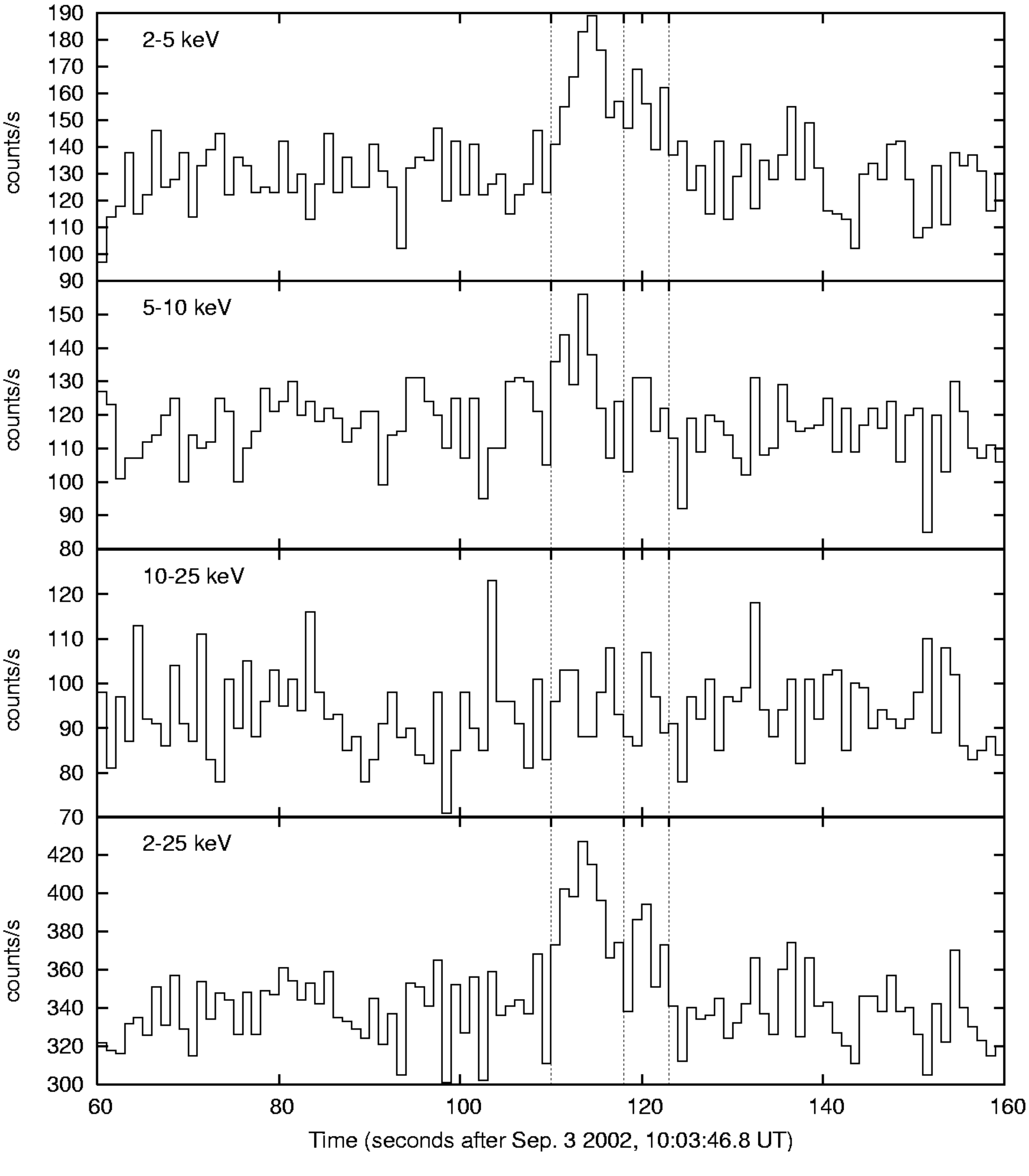

Fig. 2.— The light curve of XRF 020903 in four WXM energy bands: 2-5 keV, 5-10 keV, 10-25 keV, and 2-25 keV (top to bottom). The light curve is binned in one second bins. The vertical dotted lines show the 0 - 8 and 8 - 13 second time intervals bracketing the first and second peaks of the burst light curve. We have performed model fits to the spectra of the burst during these two time intervals, and to the entire duration of the burst (0 -13 seconds).

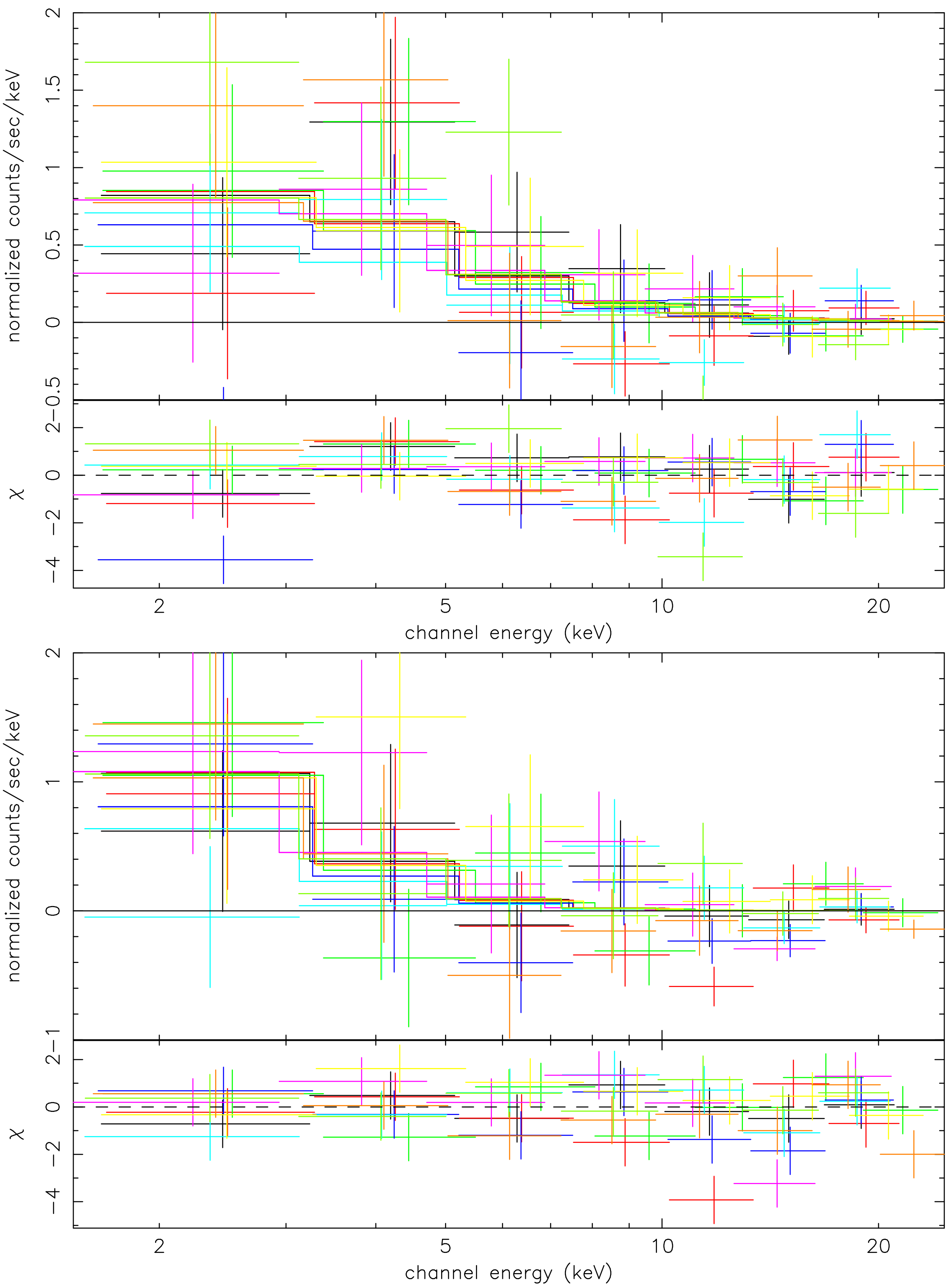

Fig. 3.— Comparison of the WXM spectra for the time intervals 0-8 and 8-13 s. The observed (crosses) and predicted (histogram) count rates are shown in a different color for each of the seven WXM wires that we have included in the fits. The spectral model is a power law with fixed photoelectric absorption (see Table 2).

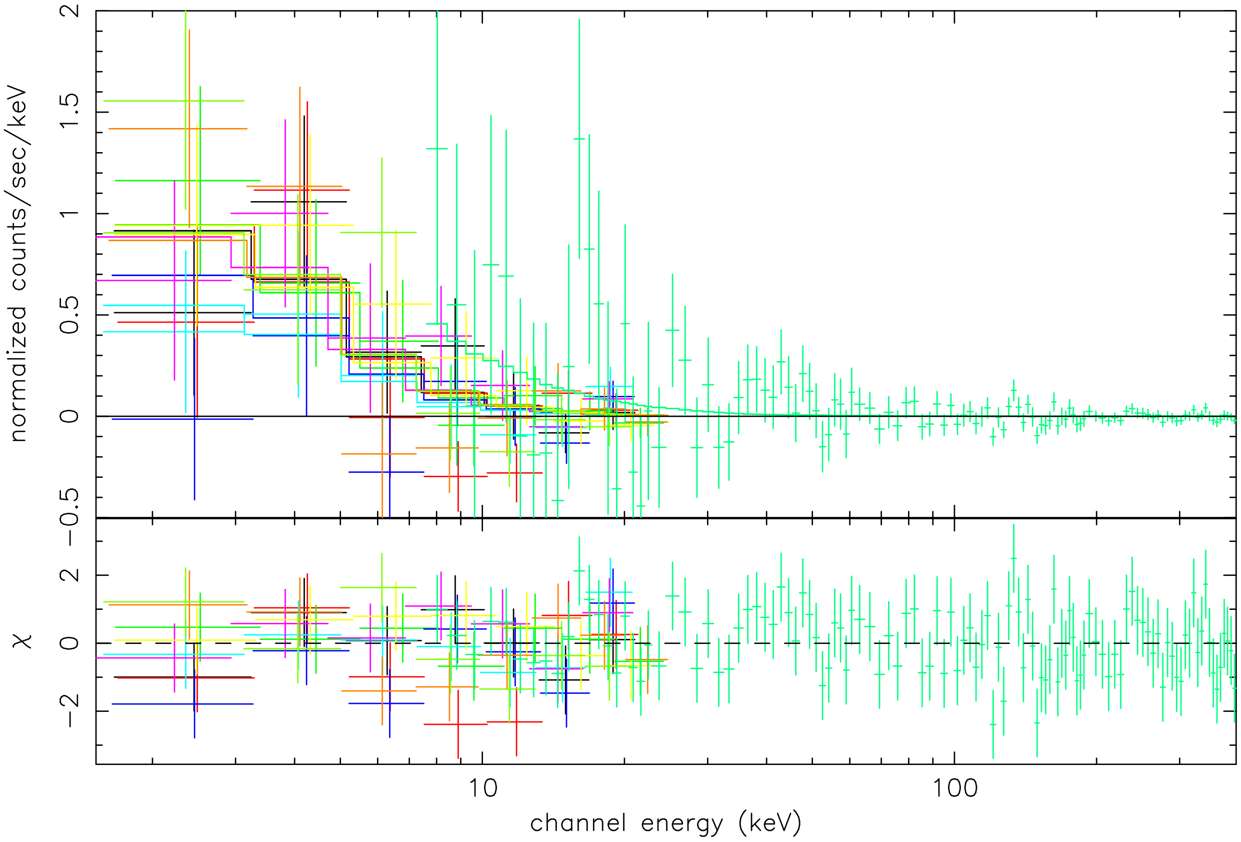

Fig. 4.— The WXM and FREGATE spectra for the entire time interval 0-13 s. The observed (crosses) and predicted (histogram) count rates are shown in a different color for each of the seven WXM wires that we have included in the fits. The spectral model is a power law with fixed photoelectric absorption (see Table 2).

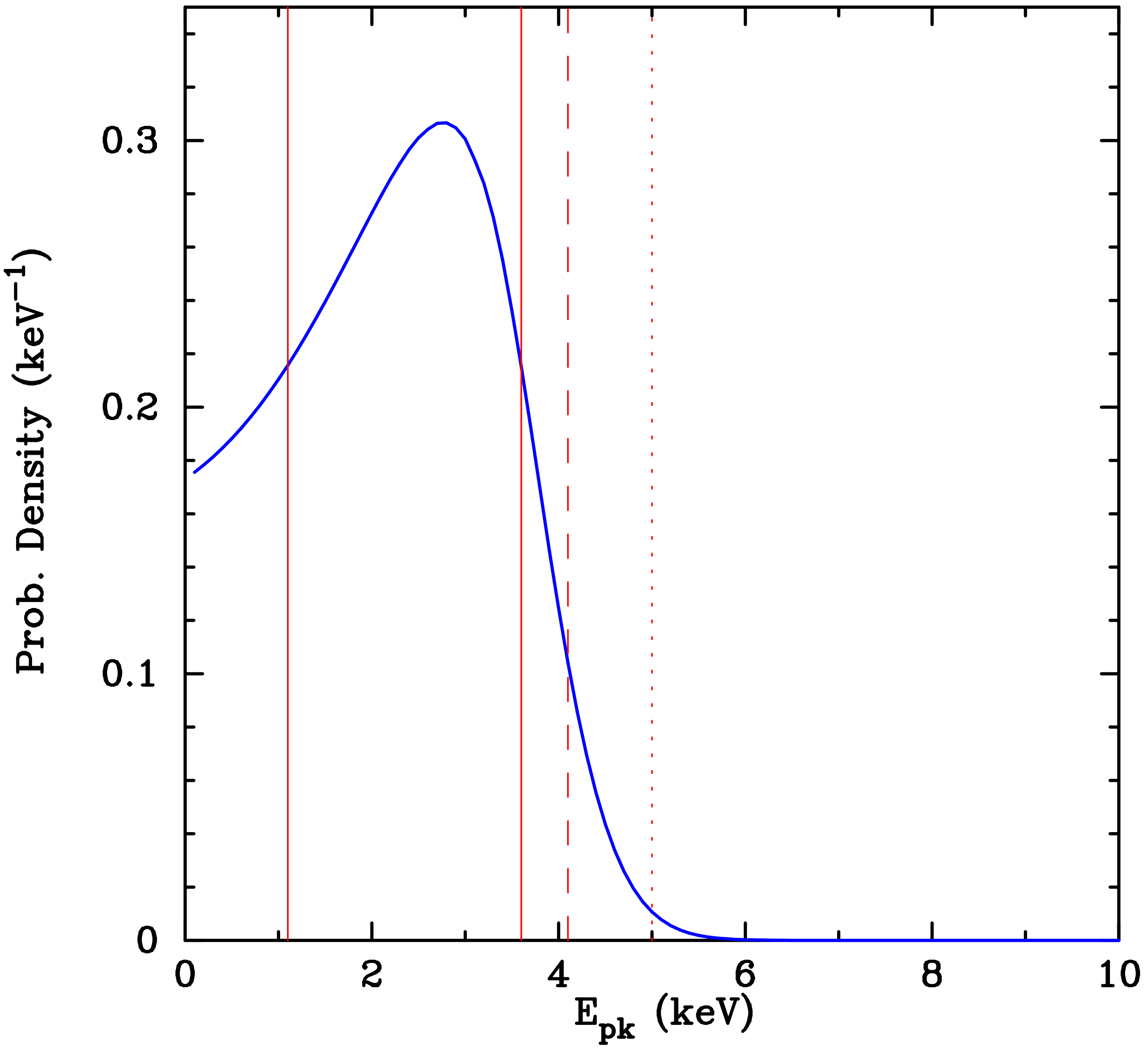

Fig. 5.— The posterior probability density distribution for $E^{\rm obs}_{\rm peak}$. The vertical solid lines define the 68% probability interval for $E^{\rm obs}_{\rm peak}$, while the dashed and dotted lines show the 95% and 99.7% probability upper limits on $E^{\rm obs}_{\rm peak}$. We find a best-fit value $E^{\rm obs}_{\rm peak} = 2.7$ keV, that 1.1 keV $< E^{\rm obs}_{\rm peak} <$ 3.6 keV with 68% probability, and that $E^{\rm obs}_{\rm peak} <$ 4.1 and 5.0 keV with 95% and 99.7% probability.

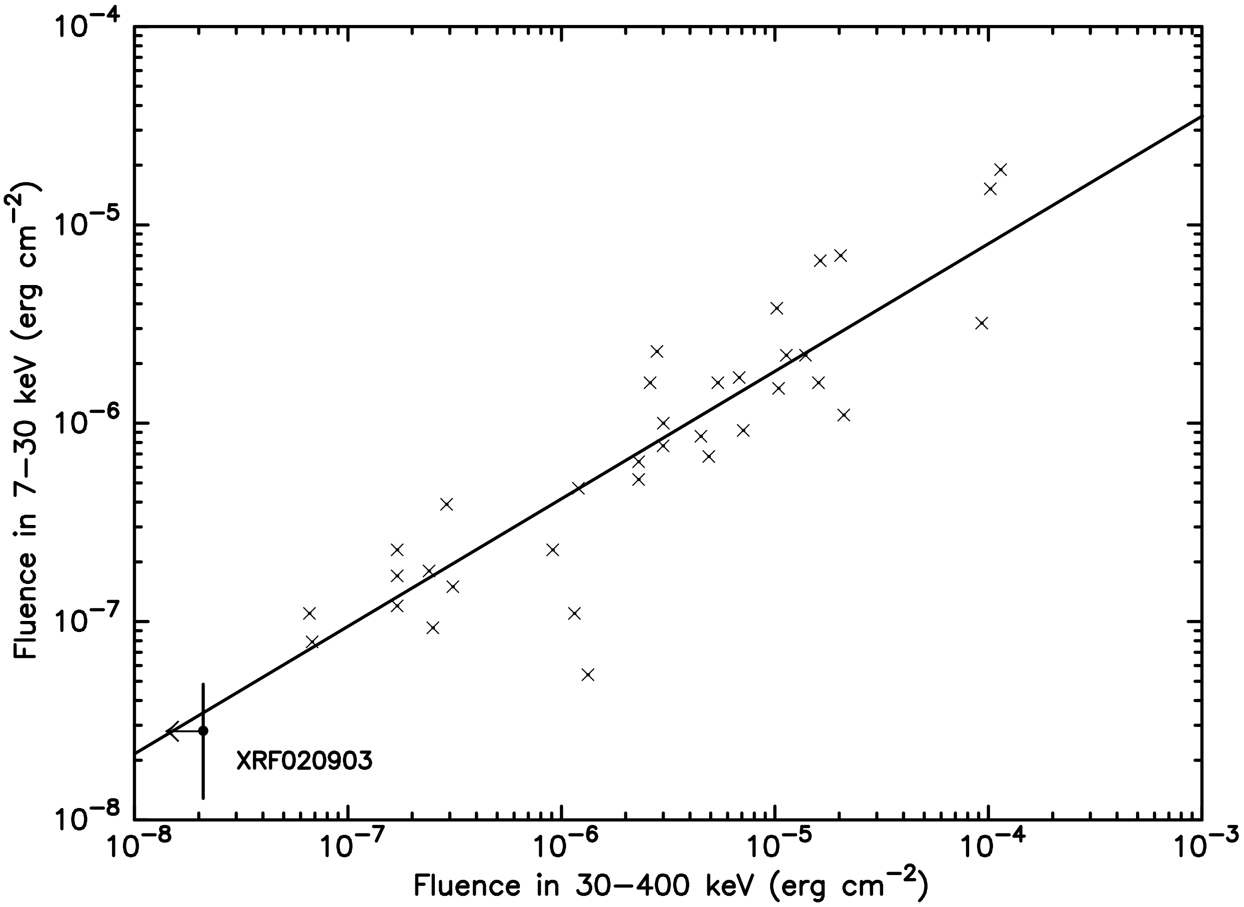

Fig. 6.— The (S_{7-30},S_{30-400})-plane, showing the location of XRF 020903, using the extrapolated total fluence in the 7-30 keV energy band and the 3σ upper limit in the 30-400 keV energy band (filled circle). The crosses are the locations of the 35 HETE/FREGATE GRBs studied by Barraud et al. (2003). The solid line is the relation, $S_{7-30} = 3 \times 10^{-3}\ \mathrm{S}_{30-400}^{0.643}$, found by Barraud et al. (2003). The properties of XRF 020903 are consistent with this relation.

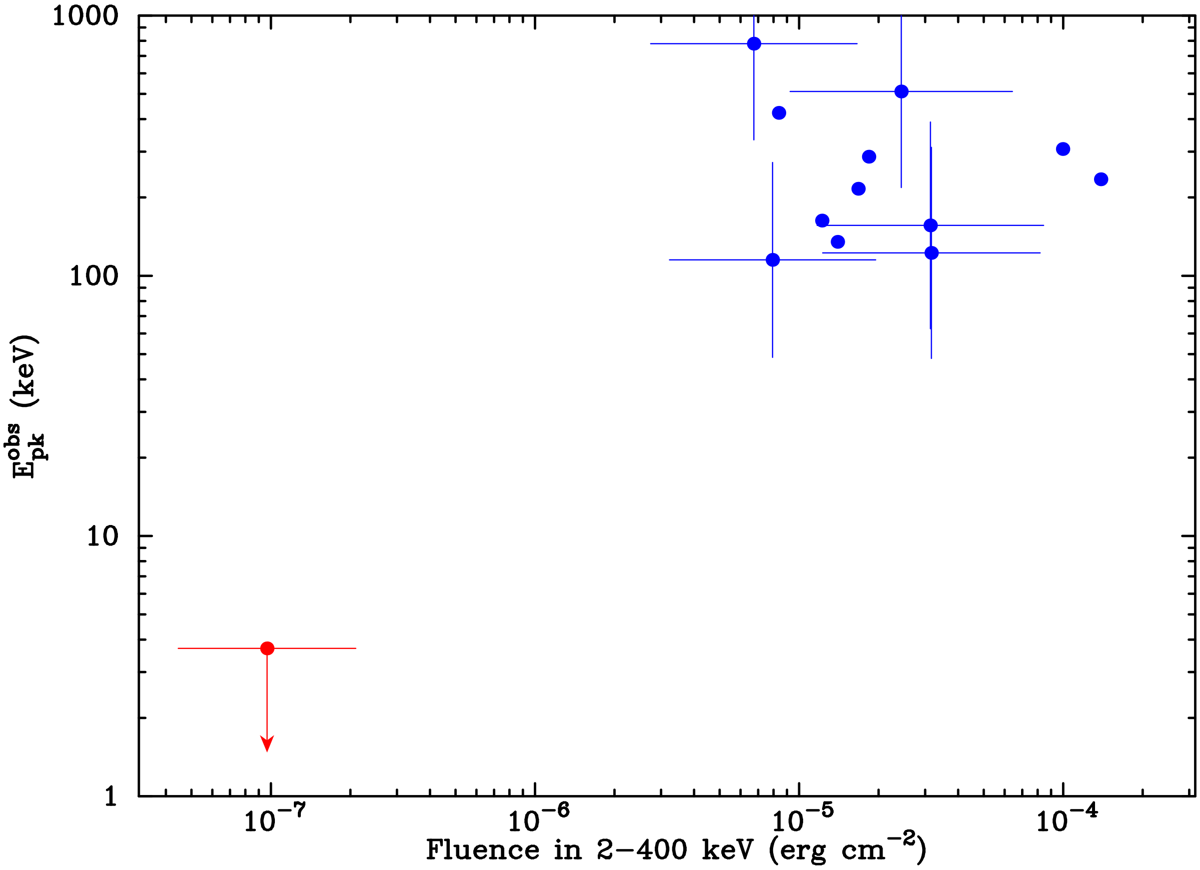

Fig. 7.— The (S_{2-400},$E_{\rm peak}^{\rm obs}$)-plane, showing the location of XRF 020903. For $E_{\rm peak}^{\rm obs}$, we plot the 99.7% probability upper limit (5.0 keV). The crosses show the locations of 12 of the HETE-2 GRBs studied by Barraud et al. (2003) for which $E_{\rm peak}^{\rm obs}$ is relatively well determined. The properties of XRF 020903 are consistent with an extension by two decades of the hardness-intensity correlation found by Barraud et al. (2003).

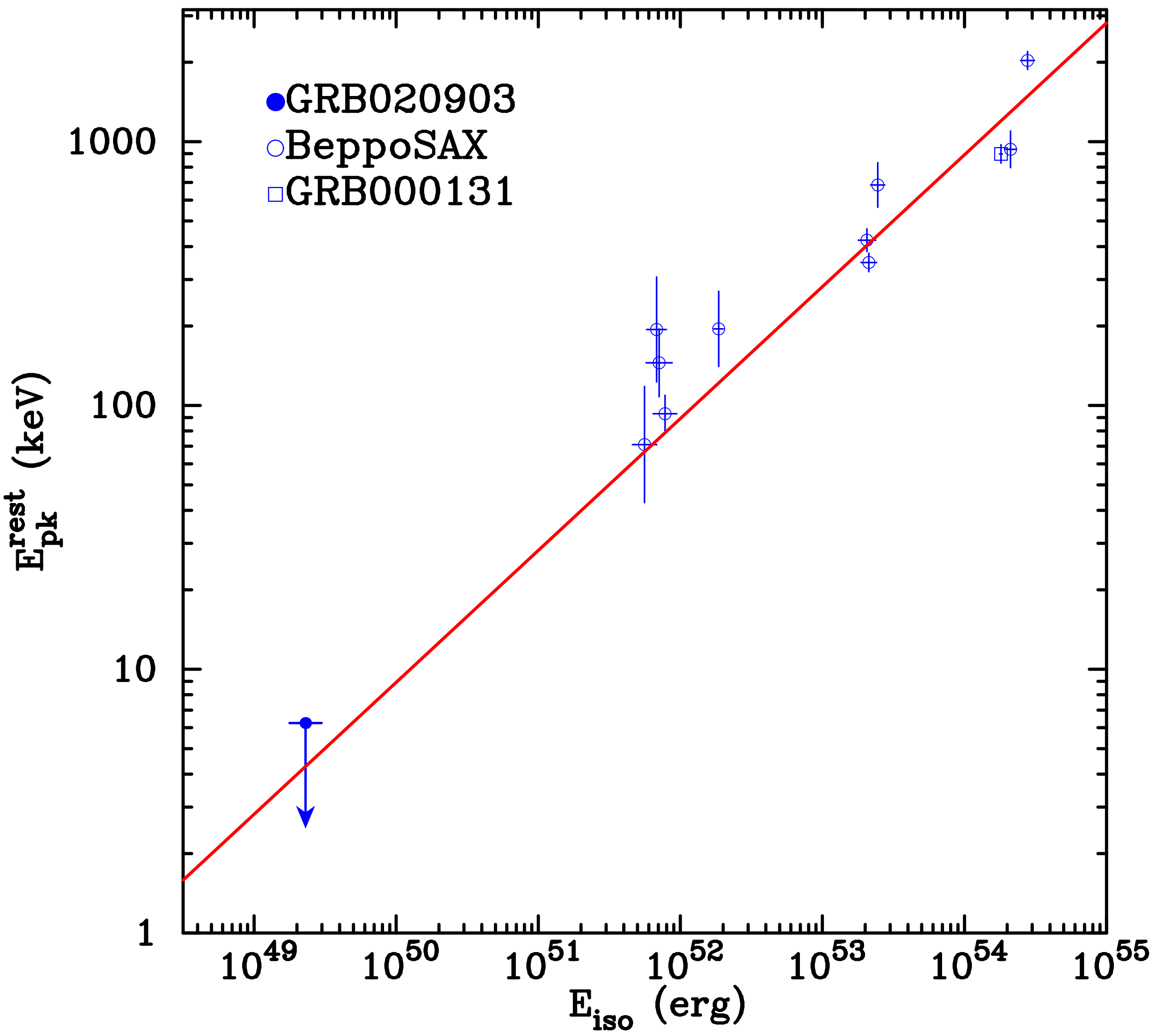

Fig. 8.— The ($E_{\rm iso}$,$E_{\rm peak}$)-plane, where $E_{\rm iso}$ is the isotropic-equivalent radiated energy between 1-10^4 keV and $E_{\rm peak}$ is the peak of the νF_ν spectrum, both measured in the rest frame of the burst. The filled circle in the lower left-hand corner is the location of XRF 020903. The ten open circles are the *Beppo*SAX GRBs reported by Amati et al. (2002). The solid line is given by the equation, $E_{\rm peak} = 89(E_{\rm iso}/10^{52}{\rm erg})^{0.5}$ keV. The properties of XRF 020903 are consistent with an extension of this relation by a factor ~ 300.

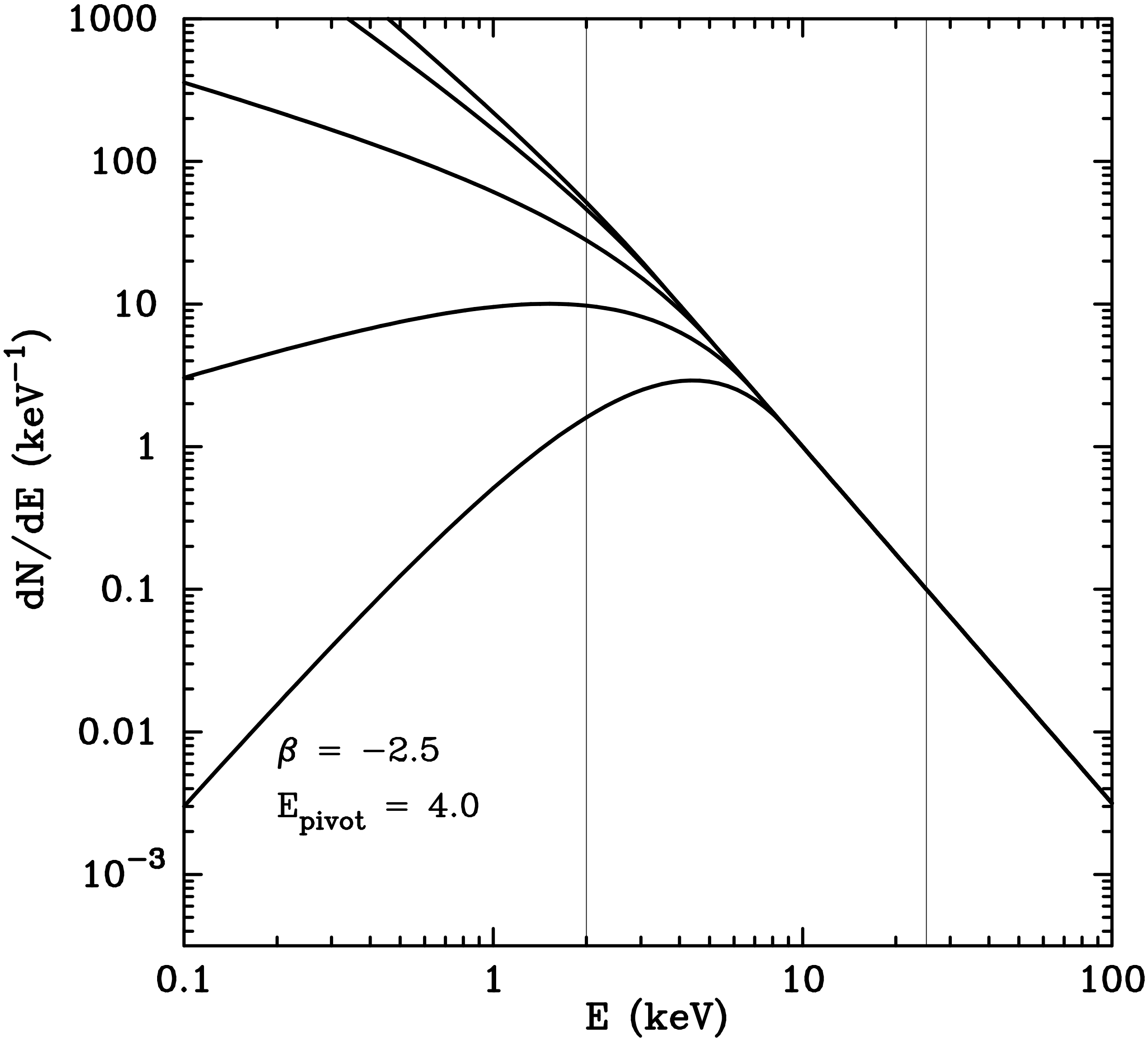

Fig. 9.— Constrained Band functions, with $\beta = -2.5$ and $E_{\rm pivot} = 4$ keV, for different values of $E_{\rm peak}$. All functions have been normalized to 1 keV^{-1} at 10 keV. The two vertical lines at 2 keV and at 25 keV show the WXM bandpass. The spectra shown are (decreasing monotonically from the top at low energy), $E_{\rm peak}$ =1 keV, 2 keV, 4 keV, 6 keV, and 8 keV, respectively. As $E_{\rm peak}$ increases, $E_{\rm break}$ also necessarily increases, so that E_0 is forced to smaller and smaller values by the constraint, increasing the curvature and the value of α.

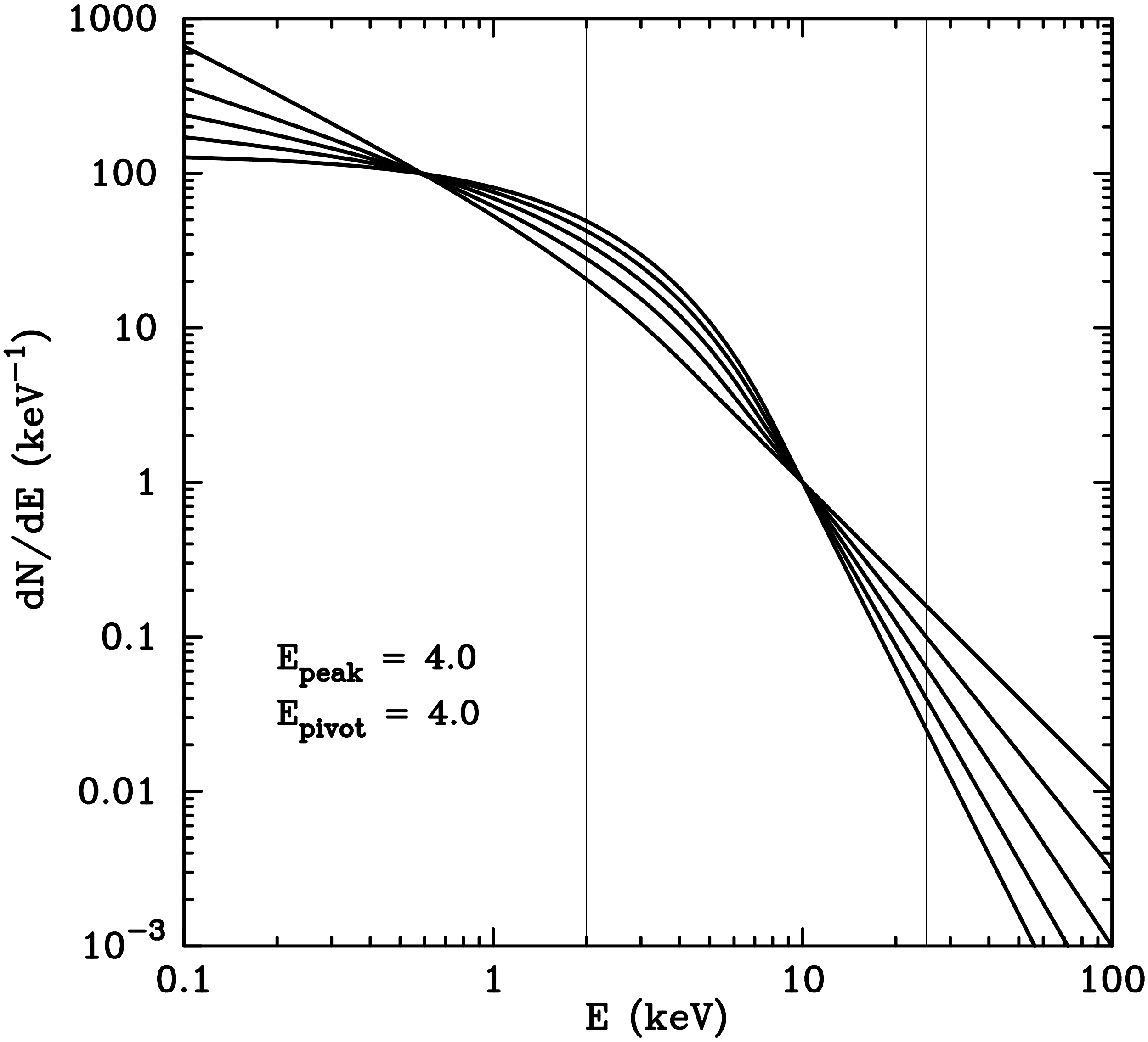

Fig. 10.— Constrained Band functions, with $E_{\rm peak} = 4$ keV and $E_{\rm pivot} = 4$ keV, for different values of β. All functions have been normalized to 1 keV^{-1} at 10 keV. The two vertical lines at 2 keV and at 25 keV show the WXM bandpass. The spectra shown are for β = -2.0, -2.5, -3.0, -3.5, and -4.0, which can be distinguished by the increasing steepness of their slopes at high energy. The progression from some curvature at low energy ($\beta = -2.0$) to almost none ($\beta = -4.0$) is evident, as is the fact that as the curvature disappears, the resulting power-law is produced by the high-energy part of the Band function.

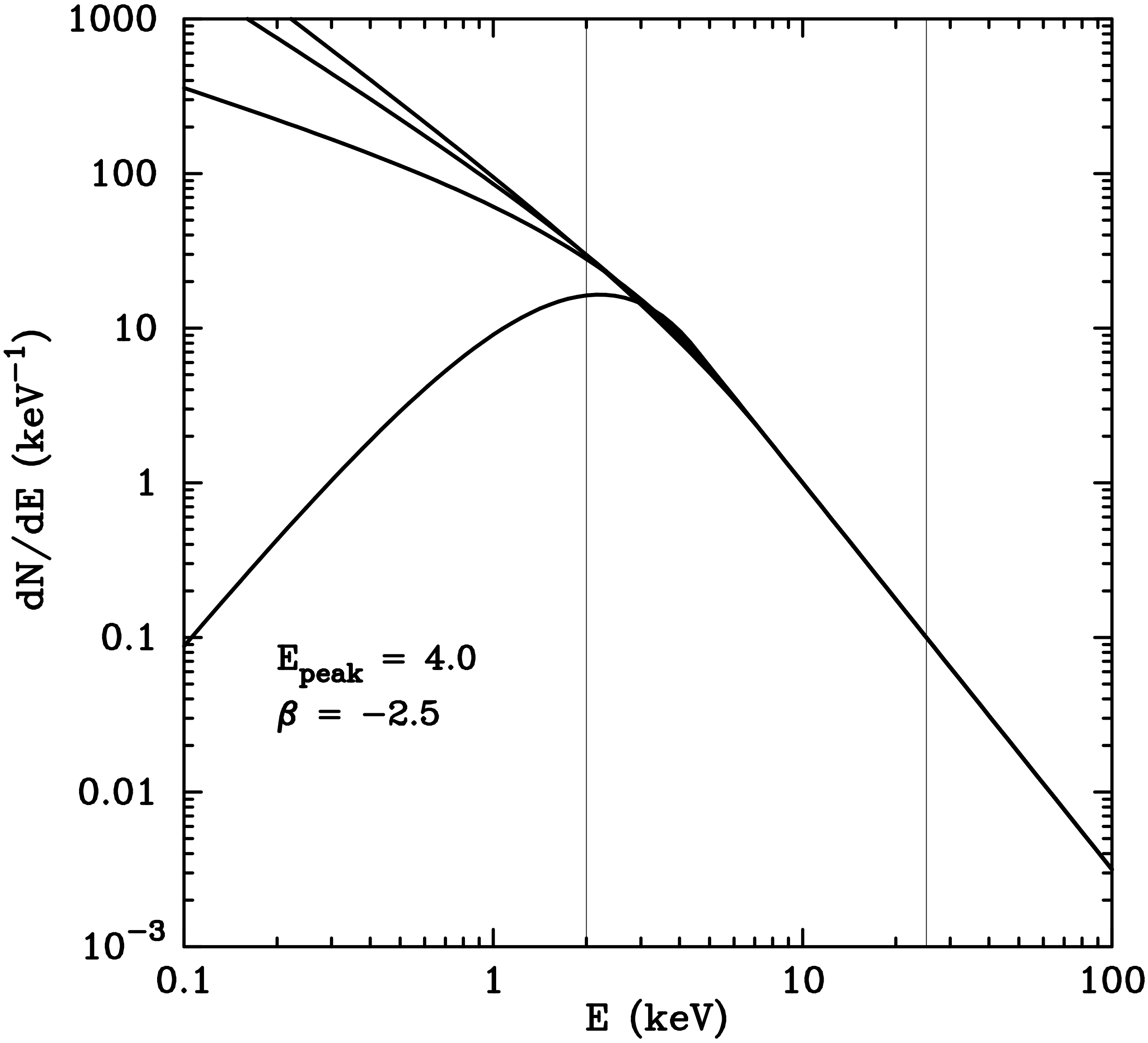

Fig. 11.— Constrained Band functions, with $E_{\rm peak} = 4$ keV and $\beta = 2.0$, for different values of $E_{\rm pivot}$. All functions have been normalized to 1 keV^{-1} at 10 keV. The two vertical lines at 2 keV and at 25 keV show the WXM bandpass. The spectra shown are (increasing monotonically at low energy) for $E_{\rm pivot} = 2$ keV, 4 keV, 6 keV, and 8 keV, respectively. Once again, as the low-energy curvature disappears, the resulting power-law is produced by the high-energy part of the Band function. Note also that the shape of the constrained Band function is insensitive to the specific choice of $E_{\rm pivot}$ within a reasonable range.

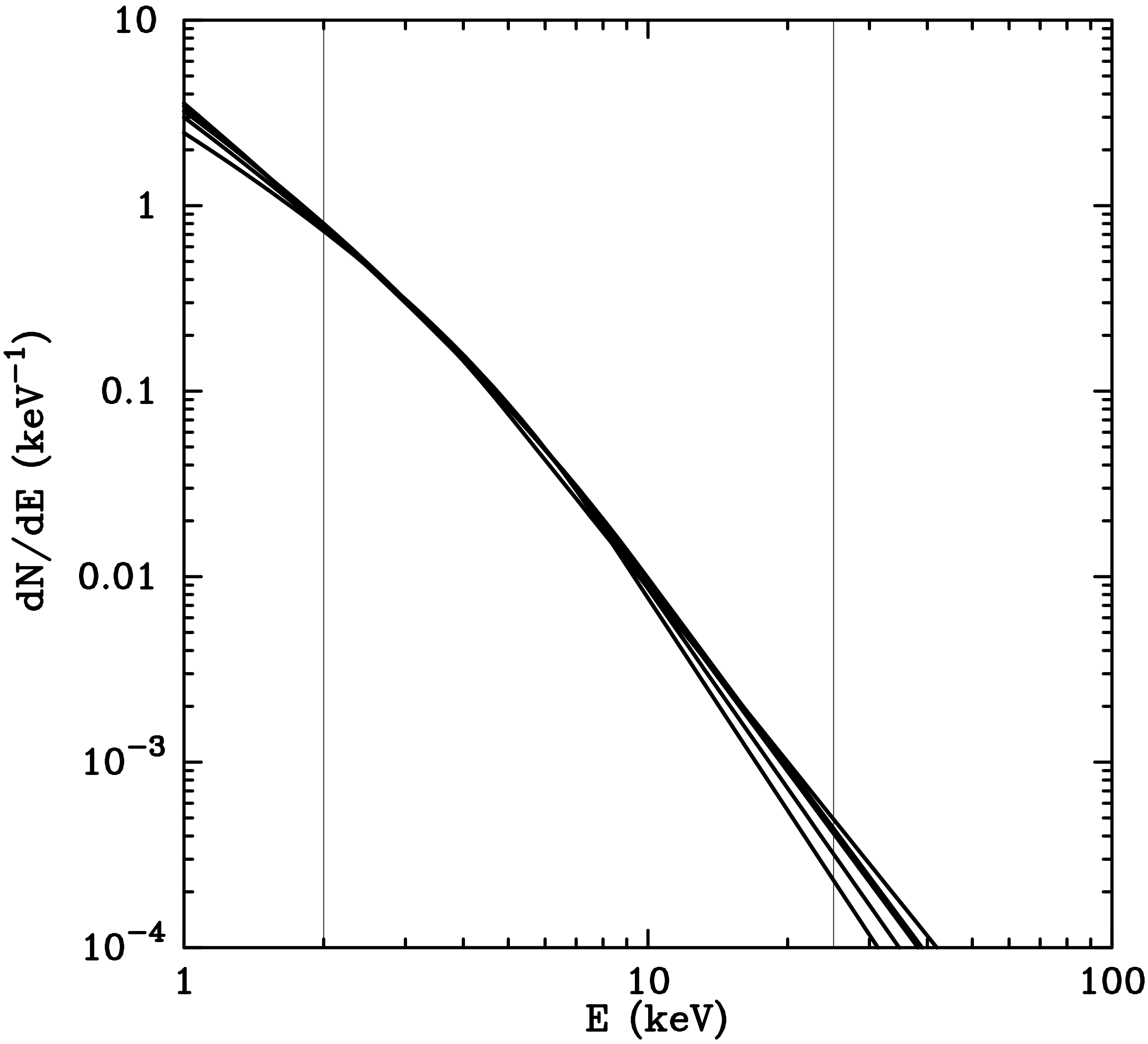

Fig. 12.— Constrained Band functions with parameters that best fit the 13 s spectrum of XRF020903, for different fixed values of $E_{\rm pivot}$. The two vertical lines at 2 keV and at 25 keV show the WXM bandpass. All functions have been normalized so that the integral from 2 keV to 25 keV is one photon. The five spectra shown in the plot corresponding to $E_{\rm pivot} = 4$ keV, 5 keV, 6 keV, 7 keV, and 8 keV (the 7 keV and 8 keV largely overlap each other). This figure illustrates a robust aspect of the constraint procedure: the best-fit model is essentially unchanged in the WXM spectral band despite a factor-of-two change in the value of $E_{\rm pivot}$.